

Growing Structure Based on Viscous Actuation of Constrained Multistable Elements

Ezra Ben Abu, Yaron Veksler, Shai Elbaz, Anna Zigelman, and Amir D. Gat*

Growing soft materials which follow a three dimensional (3D) path in space are critical to applications such as search and rescue and minimally invasive surgery. Herein, a concept for a single-input growing multi-stable soft material, based on a constrained straw-like structure is presented. This class of materials are capable of maneuvering and transforming their configuration by elongation while executing multiple turns. This is achieved by sequenced actuation of bi-stable frusta with predefined constraints. Internal viscous flow and variations in the stability threshold of the individual cells enable sequencing and control of the robot's movement so as to follow a desired 3D path as the structure grows. A theoretical description of the shape and dynamics resulting from a particular set of constraints is derived. To validate the model and demonstrate the suggested concept, experiments of maneuvering in models of residential and biological environments are presented. In addition to performing complex 3D maneuvers, the tubular structure of these robots may also be used as a conduit to reach inaccessible regions, which is demonstrated experimentally.

man-made disaster sites, where a survivor might be trapped below a pile of porous debris with limited oxygen or water, and minimally invasive surgery^[3–5] such as intravascular catheterization procedures. The inherently large number of degrees of freedom of these robots makes their actuation challenging. Additionally, following complex paths often requires passing through intricate narrow cavities and networks, so these robots have to be slender in order to accomplish this. Slenderness, however, typically limits a robot's ability to move forward and to turn rapidly due to the friction that develops when pushing it forward.

Growing materials, lengthening from the tip, involve no relative movement of the body with respect to the terrain. For slender growing materials with strong friction, this provides a convenient solution allowing the robot to

1. Introduction


We present a growing and maneuvering multi-stable soft material; on the sequential activation of constrained bi-stable frusta via viscous flow from a single input. The tubular structure of the robot allows it to transfer materials to unreachable regions, via an internal channel. The constraints define the final configuration of the robot, and the viscous flow allows a sequenced actuation of the straw elements, which enables the robot to follow a desired 3D path as the structure grows.

Growing materials' ability to travel along 3D paths in space is fundamental to their utility. Advancing along a 3D path and avoiding obstacles within complex environments is common in applications such as search and rescue missions^[1,2] in natural or

maneuver by elongation in complex environments. One example of such robots, which are able to navigate inside a 3D maze through growing, was proposed by Hawkes et al.^[6] in the context of inverted thin-walled vessels. This concept was also extensively studied by others for various applications.^[7–14]

As mentioned above, slender growing materials inherently involve an extremely large number of degrees of freedom. Thus, a major challenge in soft robotics is to simplify the robot's actuation, reducing the required control mechanisms. The development of strategies for efficient actuation and control of growing soft robots is essential to the advancement of the field. For instance, a single input actuation was investigated for example, by Mosadegh et al.,^[15] who used a pneumatic-network, which consists of small channels in elastomeric materials. Yang et al.^[16] proposed the design of a "single-unit buckling actuator" which consists of an elastomeric structure with a "nonbuckling center area" connecting to several "buckling pillars." Later on, Jin et al.^[17] proposed a design of multi-functional robots that operate with a single pressure input and without the need for electronic components. In particular, they utilized viscous flow and snapping arch principles, fully integrated on-board, enabling the control of the incoming airflow. Another design incorporating the interplay between bi-stability and soft actuators, was suggested by Gorissen et al.^[18] for a single-input jumping robot, where the snapping of elastomeric spherical caps upon pressurization results in a sudden release of energy which leads to a rapid jump. Flow-based sequenced actuation of multiple bi-stable elements was studied by Ben Haim et al.,^[19] who provided a closed-form

E. Ben Abu, Y. Veksler, S. Elbaz, A. Zigelman, A. D. Gat
Faculty of Mechanical Engineering
Technion - Israel Institute of Technology
Haifa 3200003, Israel
E-mail: amirgat@technion.ac.il

 The ORCID identification number(s) for the author(s) of this article can be found under <https://doi.org/10.1002/admt.202202184>

© 2023 The Authors. Advanced Materials Technologies published by Wiley-VCH GmbH. This is an open access article under the terms of the Creative Commons Attribution License, which permits use, distribution and reproduction in any medium, provided the original work is properly cited.

DOI: 10.1002/admt.202202184

model for the dynamic control of multiple bi-stable hyperelastic balloons. A design for growing soft-robot with a single actuation input was proposed by Connolly et al.,^[20] who focused on fiber-reinforced actuators, where for a given trajectory, they found the optimal design parameters for an actuator.

Here, we present a growing and maneuvering multi-stable structure based on the sequential activation of bi-stable elements via viscous flow. As the multi-stable structure, a commercially available straw composed of a sequence of conical frusta is a convenient and natural candidate. The bi-stability of the conical frusta, resulting in a multi-stability of the straw-shaped structures, was studied by Bende et al.,^[21] who linked the geometry and internal stress properties to multi-stable functionality in the bending and extension states. Most recently, Breitman et al.,^[22] investigated the fluid-solid-interaction dynamics occurring in a multistable straw filled with highly viscous fluid. Other multi-stable truss structures with similar properties to those of conical frusta were recently investigated by Hua and coworkers,^[23] as well.^[24,25]

The purpose of this study is to explore how viscous flow and a constrained slender multi-stable structure can be leveraged to accomplish controlled growth and maneuvering of multi-stable growing material using sequential activation of bi-stable elements. Below, we derive a theoretical description of the shape and dynamics resulting from a particular set of constraints. Models of residential and biological environments are used to experimentally demonstrate the robot's ability to perform complicated 3D maneuvers and a variety of additional operations such as heart structural intervention and fire extinguishing.

2. Results

We suggest leveraging internal viscous flow in a single-input multistable growing material to achieve controlled sequenced actuation and growth-based locomotion in a complex 3D environment. As a model for manipulation and control of the proposed robot, we chose a straw-like structure, see **Figure 1A**, which is a common, fluid-sealed, and slender multistable structure. In order to maneuver in a complex environment, it is essential to steer while elongating, which may be achieved by creating asymmetric constraints in different segments of the straw. Such constraints can be created by using various methods, and for the current configuration polypropylene sheets were soldered in the desired regions (see Experimental Section), marked by black lines in **Figure 1A**, which hold one side of the straw closed.

2.1. Using Viscous Effects to Minimize the Swept Area via Sequencing

In **Figure 1A**, we show an example of a planar path (marked by a dashed black curve), along with the straw configuration at different times during its growth. The path determines the positions of the constraints, as well as the number of frusta that are stitched together at each location. For the current configuration, each frustum allows the steering angle of $\approx 16^\circ$. Using straws with a different frustum length or a different outer diameter allows various resolutions of the steering angle. We note that before the straw

steers in a given direction, the front (closed frusta region) deviates from the desired path. During the propagation along the desired path, this deviation decreases, since fewer closed frusta are left in the straw.

We define the *swept area* as all locations which the soft-robot occupied during the process of growth to its final state. To follow a 3D path accurately, the swept area should be minimized, ideally to only the final 3D path. In **Figure 1** panels (B1) and (B2) we show the results of planar kinematical simulations (kinematic analysis section) of the constrained straw where the constraints' locations and the number of constrained frusta were dictated by the desired final configuration. **Figure 1** compares simulations of the swept area for both sequenced actuation (B1) and random actuation (B2). It can be seen that the swept area in **Figure 1 B1** is much smaller than in **Figure 1 B2**, demonstrating the importance of a sequenced actuation to accurately grow along a predefined path. This result is also verified experimentally (Movie S1, Supporting Information) in **Figure 1 C1** (viscous fluid based sequenced actuation) and **Figure 1 C2** (air pressurization leading to random actuation). More data on the experimental parameters are available in the Experimental Section below.

2.2. The Effect of Constraints on the Stability Threshold

In **Figure 1** panel (E) we show the pressure in the straw, P , versus the experimentally measured values of the frustum elongation, L , for experiments with and without constraints. All straws contained six frusta, and for the constraint experiments, the straw was bent in each frustum by right-left-right-left-right-left, so that overall, its elongation was forward. We denote the upward snapping pressures by P_{s-b}^{up} (0.3 atm) and P_{s-f}^{up} (0.22 atm), which are the minimum pressure values needed for opening one frustum, with and without a constraint ("b" represents constrained elongation during bending and "f" represents unconstrained forward only elongation), respectively. Similarly, the downward snapping pressures denoted by P_{s-b}^{down} (-0.08 atm) and P_{s-f}^{down} (-0.1 atm), represent the maximum pressure values needed for closing one frustum, with and without a constraint. In all measurements, the standard deviation of the snapping pressure is below 0.01 atm.

It can be seen that, the constraints affect the threshold of stability, since $P_{s-b}^{up} > P_{s-f}^{up}$ and $P_{s-b}^{down} < P_{s-f}^{down}$, this implies that if the applied pressure is in the range ($P_{s-f}^{up}, P_{s-b}^{up}$). Then only the unconstrained frusta will open and the constrained ones will remain closed and if the applied pressure is in the range ($P_{s-b}^{down}, P_{s-f}^{down}$) only the constrained frusta will close and the unconstrained ones will remain open. On the other hand if the applied pressure is equal to or greater than P_{s-b}^{up} , then the unconstrained frusta will open first, and afterward the constrained ones. Furthermore, the graph in **Figure 1** panel (E) presents that the elongation of the constrained frusta is reduced by a factor of two relative to the unconstrained ones. In addition, the ratio between the unstable regions slopes k_{s-b} and k_{s-f} , for the constrained and unconstrained frusta, respectively, is approximately 2.5, specifically $k_{s-b} \approx -27,000 \text{ kPa} \times \text{m}^{-1}$ and $k_{s-f} \approx -11,000 \text{ kPa} \times \text{m}^{-1}$. This observation is important for modeling and controlling this system, and particularly for demonstrating that, in the case of negligible viscous effects, the frustum without a constraint opens before the frustum with a constraint.

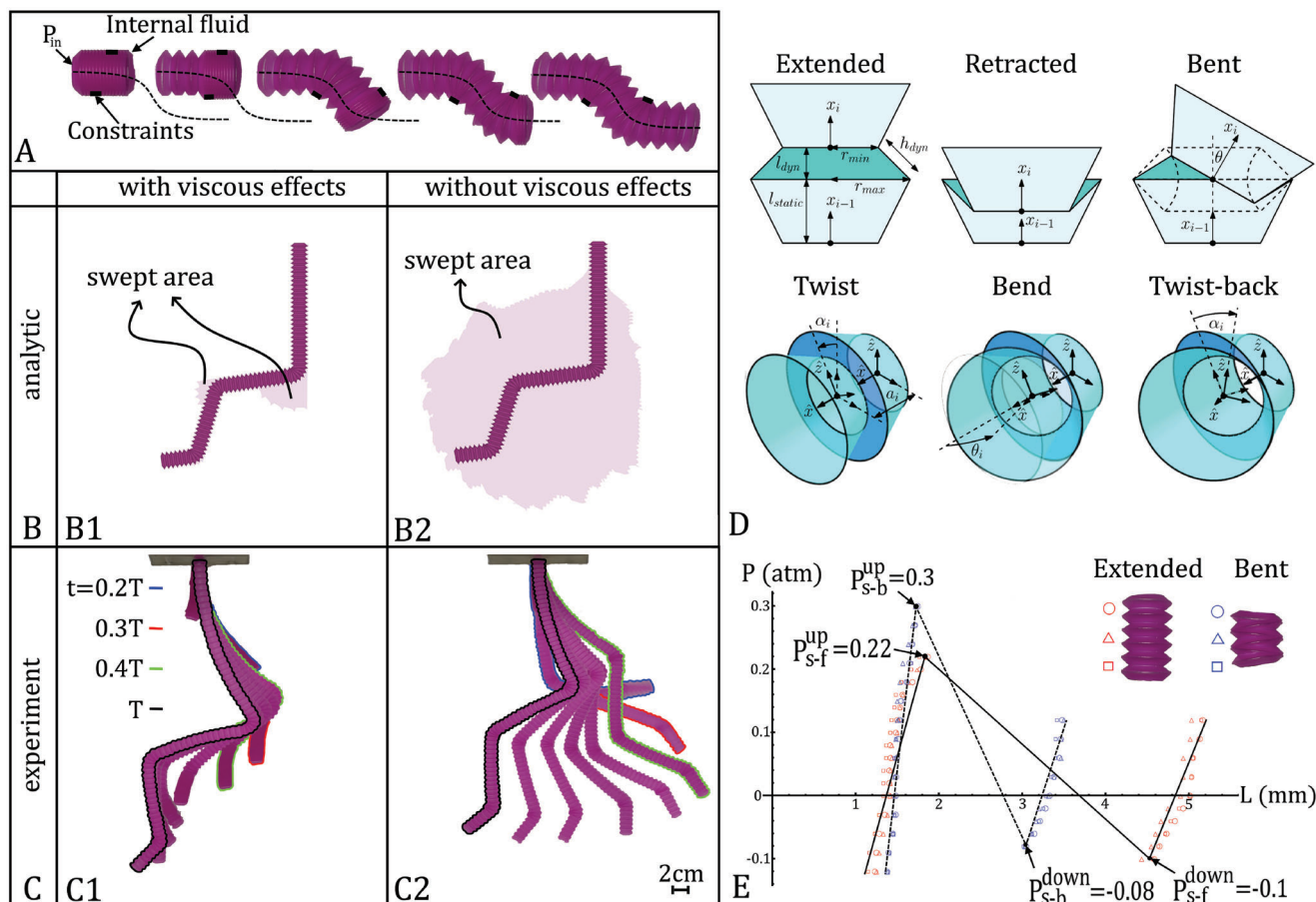


Figure 1. Demonstration of growth of a multistable structure along with schematic sketches of all possible configurations and mechanical properties. A) The growth of a straw-like structure with constraints (marked by black continuous lines). The sequenced opening of the bi-stable elements which results in growth along a pre-defined path (marked by a black dashed line). Panels (B1) and (B2) present kinematic simulations for sequenced growth (viscosity dominated dynamics) and unordered growth (negligible viscosity), respectively, where the pink regions denote the swept area, defined as all regions which the structure passed through during the growth process. Panels (C1) and (C2) present experimental results for actuating the configurations by a viscous internal fluid (silicone oil with viscosity of $60 \text{ Pa} \times \text{s}$) at times, $t = 0.2T, \dots, T$, where $T = 6 \text{ s}$, and by an inviscid internal fluid (air) at times, $t = 0.2T, \dots, T$, where $T = 2 \text{ s}$, respectively. D) Illustration of detailed descriptions for all possible element's configurations. E) Experimental measurements of stiffness of different states and stability thresholds. Experimental data showing the internal pressure in the straw, P versus the frustum elongation, L , corresponding to retracted-extended snap-through (red markers) and retracted-bent snap-through (blue markers). The different markers indicate different experiments and straws. The frustum length was calculated by measuring the average elongation of six connected frusta. The scale bar corresponds to 2 cm.

2.3. Relating the Constraints Positions to the Growth Kinematics

A straw-structure can be viewed as a 1D lattice composed of multi-stable elements. Each element is constrained to a small set of possible states, where the states may be obtained by different geometric transformations. These transformations can generally be divided into three categories: i) retracted element; ii) extended element; and iii) bent element (see Figure 1D). To describe the full kinematics of the entire structure, a local coordinate system is prescribed for each element. These local coordinate systems may be defined according to the Denavit–Hartenberg notation,^[26] where the local axial direction of the element is x , whereas the z -axis lays in the cross-section of the element (see Figure 1D). To transform one coordinate system into another, the following transformation matrix is used,

$${}^i T_j = \begin{bmatrix} Rot_{3 \times 3} & Trans_{3 \times 1} \\ 0_{1 \times 3} & 1 \end{bmatrix} \quad (1)$$

where $Rot_{3 \times 3}$ is a rotation matrix, $Trans_{3 \times 1}$ is a translation vector, and $0_{1 \times 3}$ is a vector of zeros. For a serial structure, it is usually straightforward to construct the transformation matrix between two consecutive elements' coordinate systems. Hence, to transform the world coordinate system into an element's coordinate system, one must multiply all previous local transformation matrices

$${}^w T_i = {}^w T_0 \cdot {}^0 T_1 \cdot {}^1 T_2 \cdot \dots \cdot {}^{i-1} T_i \quad (2)$$

The local transformation from element $(i - 1)$ to element (i) , denoted by ${}^{i-1} T_i$, is comprised of a translation, a_i , along x_i

Table 1. Translation and rotation values for different straw element states.

	Retracted	Extended	Bent
a_i - Translation in \hat{x} direction	$l_{\text{static}} - l_{\text{dyn}}$	$l_{\text{static}} + l_{\text{dyn}}$	l_{static}
θ_i - Bending angle	0	0	Θ
α_i - Bending direction angle (twist)	-	-	$\in [0, 2\pi)$

($Trans_{x_i}(a_i)$) and a bending rotation with angle θ_i around an axis u_i , where the u_i -axis is located in the cross-section of element i and may be obtained by rotating z_i by an angle α_i around the x_i -axis. To compute the local transformation matrix for straw elements, we can decompose the bending rotation into three rotations (see Figure 1D). First, rotating the coordinate system around x_i with angle α_i (twist), then rotating with angle θ_i around the new z_i (bend), and finally rotating back around the new x_i with angle $(-\alpha_i)$, in order to bring the z_i -axis back to its original orientation:

$${}^{i-1}T_i = Trans_{x_i}(a_i) Rot_{x_i}(\alpha_i) Rot_{z_i}(\theta_i) Rot_{x_i}(-\alpha_i) \quad (3)$$

where the translation and rotation matrices are defined as

$$Trans_{x_i}(a_i) = \begin{bmatrix} 1 & 0 & 0 & a_i \\ 0 & 1 & 0 & 0 \\ 0 & 0 & 1 & 0 \\ 0 & 0 & 0 & 1 \end{bmatrix} \quad (4)$$

$$Rot_{x_i}(\alpha_i) = \begin{bmatrix} 1 & 0 & 0 & 0 \\ 0 & \cos(\alpha_i) & \sin(\alpha_i) & 0 \\ 0 & -\sin(\alpha_i) & \cos(\alpha_i) & 0 \\ 0 & 0 & 0 & 1 \end{bmatrix} \quad (5)$$

$$Rot_{z_i}(\theta_i) = \begin{bmatrix} \cos(\theta_i) & \sin(\theta_i) & 0 & 0 \\ -\sin(\theta_i) & \cos(\theta_i) & 0 & 0 \\ 0 & 0 & 1 & 0 \\ 0 & 0 & 0 & 1 \end{bmatrix} \quad (6)$$

The values of the parameters a_i , θ_i , and α_i depend on the geometry of the straw element and its state. The geometrical model of a straw element assumes that each element is constructed from a static frustum of length l_{static} and a dynamic frustum of length l_{dyn} , with outer radius r_{out} and inner radius r_{in} (see Figure 1D). **Table 1** summarizes the values of the transformation parameters for different element states.

The value of the bending angle Θ appearing in Table 1 can be estimated by a 2D analysis of a straw element. Assuming the outer and inner radii of the element are constant, the bending angle can be found by using the cosine rule (see Figure 1D):

$$\Theta = \arccos\left(\frac{r_{\text{out}}^2 + r_{\text{in}}^2 - h_{\text{dyn}}^2}{2 \times r_{\text{in}} \times r_{\text{out}}}\right) \quad (7)$$

where h_{dyn} is the side-length of the dynamic frustum. Assuming h_{dyn} remains constant for all element states, its value can be calculated for an element in the extended state (see Figure 1D):

$$h_{\text{dyn}}^2 = (r_{\text{out}} - r_{\text{in}})^2 + l_{\text{dyn}}^2 \quad (8)$$

A kinematic simulation of the entire straw structure was created by combining the forward kinematic computations for all straw elements, as described in Equations (1)–(6), using the parameter values for different element states as given in Table 1 and Equations (7) and (8). This simulation was then utilized to create the swept area domains for the two scenarios, which were shown in Figure 1 B1,B2. The swept area in Figure 1 B1 illustrates a sequenced elements' elongation, where all elements were transformed from a retracted state to their final state. The swept area shown in Figure 1 B2 was obtained by taking a union of 200 domains found from random-order element activation.

2.4. Demonstration of Maneuvers and Operations in Complicated 3D Environments

In **Figure 2A,B** (Movie S1, Supporting Information), we demonstrate two possible applications of the suggested concept of a controlled single-input growing material with viscous internal fluid, which maneuvers inside a 3D complex environment (a residential model and a model of human lungs-like structure). In both cases, we performed several experiments with different goal positions and recorded the straw growth. In the experiments presented below, the number of constrained frusta is in the range 6 – 16, and the average elongation was approximately 440% of the resting length. In these demonstrations, the growing multi-stable robot was able to follow desired paths which included passing through thin tubes and corridors, junctions, steep corners, narrow gates, dodging obstacles, overcoming gravity, and changing the plane of motion. In **Figure 2A**, we show locomotion via growth in a residential model for three different final goal locations (marked by a red chair). It can be seen that the number of bends slightly affects the final length, for example, when the number of bends is 16 (with overall steering angle of 256°), the length decreases from 325 mm (which is the maximal length of the straw) to 296 mm (meaning that in this case the overall steering angle of 256° results in the elongation decrease of approximately 10%). In **Figure 2B**, we demonstrate locomotion by growth in a lung-like model for three final goal locations (marked here by a red balloon). At each junction one tube splits into two different tubes, thus at generation n , ($n = 1, 2, 3, \dots$), there are 2^n tubes, which increases the complexity of the maneuvering till reaching the goal as the multi-stable structure grows and gets closer to the destination. The diameter in each generation is reduced by approximately 30%, which complicates and restricts the maneuvering abilities. In our case, $n = 3$, and at the last generation the inner tubes' diameter is 150% of the maneuvering robot's diameter.

In **Figure 3** (Movie S1, Supporting Information) we show the ability of the proposed soft-robot to maneuver and then to perform various operations, such as heart structural intervention in the heart-like structure (see **Figure 3A**) and putting out the

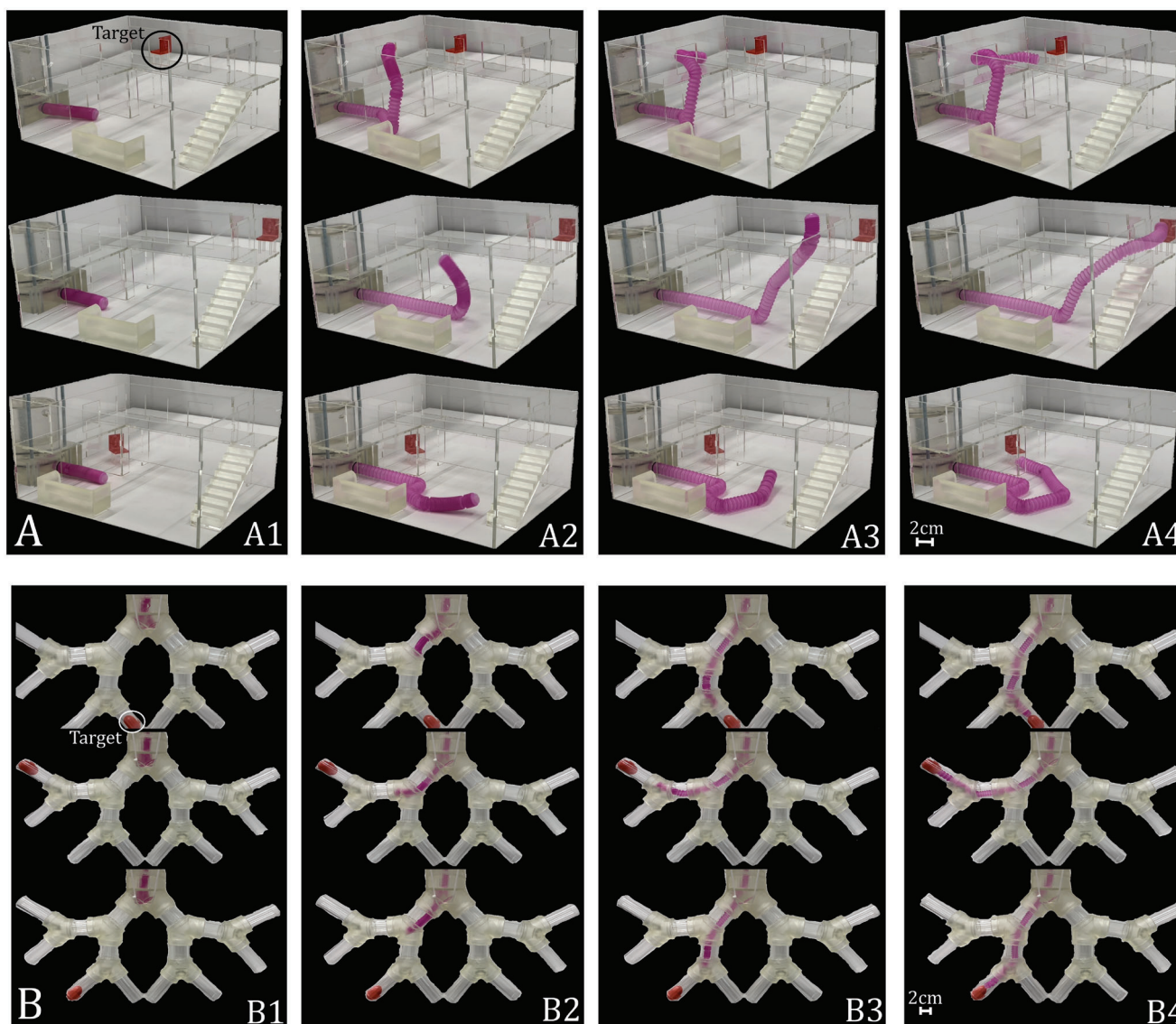


Figure 2. Growth-based maneuvering in residential and lungs-like structures. Panel (A) is a residential prototype with three different geometric targets, marked by the red chair. In each series: (A1) is the initial configuration, (A2) and (A3) are intermediate stages, and (A4) is the final configuration. The final length and the duration of the growth process are in the upper row of (A) 296 mm, 8 s, in the middle row of (A) 304 mm, 6 s, and in the lower row of (A) 292 mm, 9 s. Panel (B) is a lungs-like prototype with three different geometric targets, marked by the red balloon. The diameter of all tubes is reduced by $\approx 30\%$ at each junction and the opening angle of each junction is 130° . In each series: (B1) is the initial configuration, (B2) and (B3) are intermediate stages, and (B4) is the final configuration. The final length and the duration of the growth process are in the upper row of (B) 313 mm, 6 s, in the middle row of (B) 311 mm, 7 s, and in the lower row of (B) 313 mm, 6 s. The scale bars correspond to 2 cm.

fire in a residential model (see Figure 3B). This figure visualizes that beyond maneuvering in a 3D complex environment and reaching the goal, the soft-robot is capable of transferring various materials such as water or medical equipment. For a detailed experimental setup including the robot's cross-sectional illustration see Figure 3C, where note that the working channel is an inner tube attached to the sealed end tip of the straw allowing to transfer the above mentioned materials. The inner tube is sealed and isolated from the internal pressure inside the reservoir, and is flexible enough to move with the material as it grows.

3. Concluding Remarks

Natural phenomena as well as many engineering applications involve geometries that are narrow and complex. Maneuvering in such confined and intricate 3D environments is exceptionally challenging for conventional rigid robots. In this paper, we presented a new concept for a single-input growing material that can steer and elongate along a predefined path, as well as perform a variety of operations. In the proposed class of growing materials, we apply physical phenomena (specifically the interaction between viscosity and multi-stability) to achieve controllable

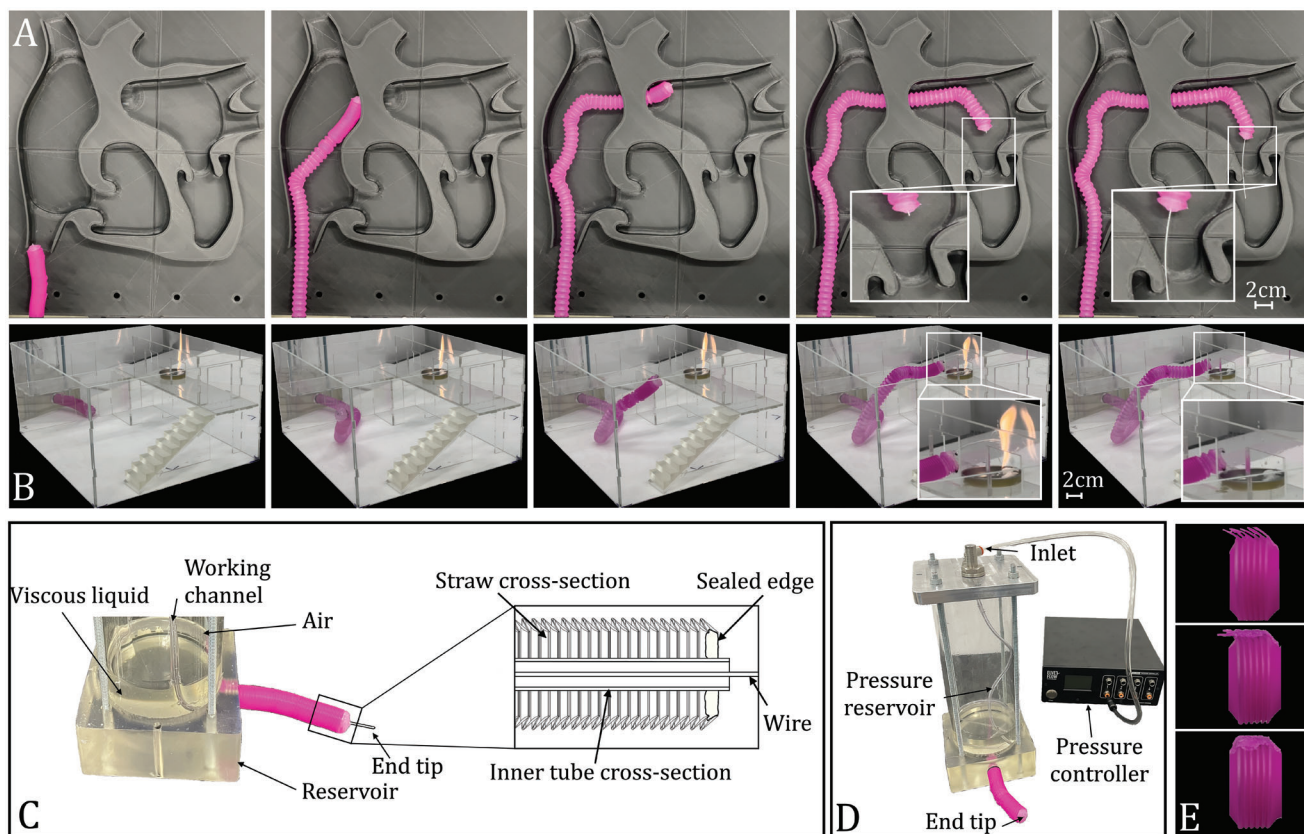


Figure 3. Maneuvering in complex environments and transferring materials to unreachable regions, via an internal channel. A) Maneuvering in a heart-like structure simulating structural heart intervention. B) Maneuvering in a residential setting and transferring water to a specific location. C) A part of the experimental setup with an enlarged view of the “end tip,” where its cross-sectional illustration is shown in the inset. D) A view of the general experimental setup which consists of a pressure controller connected by two channels to the growing material. The first channel controlled the pressure in a fluid reservoir and the second channel is used as the working channel. E) The constraints fabrication process. The scale bars correspond to 2 cm.

locomotion, enabling single-input control. The proposed growing material is a multi-stable structure with constraints located at positions computed from the kinematic analysis of the desired 3D path. We demonstrated the feasibility of the suggested concept for various scenarios. In all cases, the growing multi-stable structure was able to follow the desired path including through narrow tubes and corridors, junctions, steep corners, narrow gates, dodging obstacles, overcoming gravity, and changing its plane of motion.

Apart from viscous-based sequencing, the growing material can be controlled via utilizing the different threshold pressures for the opening of straight and bent frusta (this concept is related to ideas explored by Peretz et al.^[27] and Melancon et al.^[28]). For viscous-based sequencing, the fluidic pressure propagation determines the rate and order of opening of the frusta. The frusta are opened or closed, depending on the sign of pressure, from the inlet toward the closed end of the straw without distinction between frusta with and without constraints. In contrast, in the case of negligible viscous effects under positive pressure, we observe that frusta without any constraints open first and those with constraints close first when activated with negative pressure. This enables additional modes and geometries of the single-input growing robot. Our future directions include implementation of adaptable constraints such as magnetic constraints, which

will allow in addition to maneuvering along a pre-defined path to change the trajectory of elongation during the operations.

4. Experimental Section

Research Objective and Design: This study aimed to utilize viscous fluid interacting with multistable elastic structures to construct a simple growing material, which was capable of performing maneuvers in complex 3D environments with obstacles and junctions, such as human lungs or natural disaster sites. As a prototype for the elastic multi-stable structure, a commercially available straw was used to which constraints were attached at specific locations. Fabrication of the constraints (see Figure 3E) was accomplished with a standard soldering machine. In order to determine the constraints locations, kinematic analysis based on the desired dynamics and final configuration of the robot was used.

Fabrication of Experimental Setup: A straw made from polypropylene, which is a relatively inexpensive and convenient material for production, was used.^[29] In addition the polypropylene has a relatively high Young's modulus ($E = 1.3$ GPa) which allows to fabricate a sufficiently reliable structure. In these experiments a straw with 78 frusta was employed. At atmospheric conditions, the maximal and minimal lengths of the straw were 415 and 90 mm, respectively. Furthermore, the outer and the inner diameters of the straw were 19 and 13 mm, respectively. Generally, straw-like structures with a wide range of outer diameters (6–200 mm) are commercially available. Moreover, even smaller straws, with an outer diameter of 2 mm, can be fabricated by using standard methods.

The straw was directly attached to a fluid reservoir using a thread which is a part of the straw end. To prevent penetration, the other thread located at the second end of the straw was removed and sealed with a hot glue. In experiments with viscous fluid, the straw was filled with silicon oil (viscosity of $60 \text{ Pa} \times \text{s}$). The direct attachment between the straw and the fluid reservoir allowed to minimize the pressure losses, and therefore increases the efficiency of the system. The fluid reservoir was connected to a pressure controller (ELVEFLOW OB1 MK3+), which in turn was connected to a compressor (CompAir L07). In all experiments, the pressure controller was adjusted to $2.5 \pm 0.01 \text{ atm}$ and the temperature was kept at room temperature. In Figure 1 the straw elongation was captured by video, in 4K resolution and 240 fps, whereas in Figure 2A,B, the straw elongation was captured by video, in 1080p resolution and 30 fps, until it reached the goal.

First, after mapping the path, by the aid of the theoretical model the locations of the constraints could be found. Then the constraints were marked on the straw, on the same sides of the straw as the desired turns, for example when a right turn was to be performed, the constraint should be inserted on the right side of the straw. To elongate straight forward no constraints were needed. Then, the constraints were inserted in the appropriate zones by spreading polypropylene sheets between the neighboring frusta and soldering them together. In order to guarantee that the constraints would be perfectly adhered, the soldering machine temperature was set to $200 \text{ }^\circ\text{C}$, which was 25% higher than the melting point of polypropylene. Inserting a constraint on a single frustum results in a steering angle of approximately 16° , thus knowing in advance the desired steering angle of the maneuver, the number of adhered frusta was determined.

The lungs-like structure (see Figure 2B) consisted from Perspex tubes of length 100 mm and with inner diameters of 54, 40, and 30 mm and special connectors (printed using SLA 3D printer -Form 3B+) that fitted the tubes' diameters. The inner diameter of the inlet connector was 80 mm. The diameter of all tubes was reduced by $\approx 30\%$ at each junction and the opening angle of each junction was 130° . The lungs-like structure and the straw were attached to the bottom of the fluid reservoir. The heart-like structure (see Figure 3A) was fabricated by combining four components which were printed with FDM printer (RAISE3D pro2).

The residential model (model of a small house, see Figures 2A and 3B), was created from acrylic sheets by using a laser cutting machine (Makeblock Laserbox 40W), where the furniture was printed using SLA 3D printer (Form 3B+). The outer dimensions of the house were $250 \times 300 \times 150 \text{ mm}^3$. The height of each floor was 75 mm and the gates' dimensions were $40 \times 40 \text{ mm}^2$ and $40 \times 70 \text{ mm}^2$. The fire setup was fabricated by using a small metal can which was filled with paper soaked with IPA, and then the fire was ignited.

The pressure reservoir (see Figure 3D) used in all of the maneuver experiments was made from perspex tube, aluminium cover on top of it, and SLA printed cover on its bottom. For experiments shown in Figure 2A,B, the upper cover was used with only one pressure inlet, whereas for the experiments shown in Figure 3A an additional input inlet (working channel) was added for performing various operations such as inserting a wire for heart structural intervention or using the channel as a hydrant for splashing the water on fire. This working channel was sealed and isolated from the internal pressure inside the reservoir.

Supporting Information

Supporting Information is available from the Wiley Online Library or from the author.

Acknowledgements

This work was supported by the Ministry of Energy of Israel.

Conflict of Interest

The authors declare no conflict of interest.

Author Contributions

A.D.G. and E.B.A. conceived the research subject. E.B.A. constructed the experimental setup and conducted the experiments. Y.V. performed the theoretical analysis and numerical computations. E.B.A. analyzed the experimental data. E.B.A., Y.V., S.E., A.Z., and A.D.G. wrote the paper.

Data Availability Statement

The data that support the findings of this study are available in the Supporting Information of this article.

Keywords

growing materials, multistable structures, single-input actuation, viscous actuation

Received: January 1, 2023

Revised: March 19, 2023

Published online:

- [1] S. Han, S. Chon, J. Y. Kim, J. Seo, Dong G. Shin, S. Park, J. T. Kim, J. Kim, M. Jin, J. Cho, *IEEE Robot. Autom. Lett.* **2022**, 7, 1667.
- [2] G. Gerboni, T. Ranzani, A. Diodato, G. Ciuti, M. Cianchetti, A. Menciassi, *Meccanica* **2015**, 50, 2865.
- [3] X. Hu, A. Chen, Y. Luo, C. Zhang, E. Zhang, *Comput. Assist. Surg.* **2018**, 23, 21.
- [4] R. F. Loffroy, B. A. Abualsaud, M. D. Lin, P. P. Rao, *J. Gastrointest. Surg.* **2011**, 3, 89.
- [5] M. Runciman, A. Darzi, G. P. Mylonas, *Soft Robot.* **2019**, 6, 423.
- [6] E. W. Hawkes, L. H. Blumenschein, J. D. Greer, A. M. Okamura, *Sci. Robot.* **2017**, 2, eaan3028.
- [7] P. Auf der Maur, B. Djambazi, Y. Haberthür, P. Hörmann, A. Kübler, M. Lustenberger, S. Sigrist, O. Vigen, J. Forster, F. Achermann, E. Hampf, R. K. Katzschmann, R. Siegwart, in *Proc. of 2021 IEEE 4th Int. Conf. on Soft Robotics (RoboSoft)*, IEEE, Piscataway, NJ **2021**, p. 15.
- [8] S. K. Talas, B. A. Baydere, T. Altinsoy, C. Tutcu, E. Samur, *Soft Robot.* **2020**, 7, 521.
- [9] A. Sadeghi, E. Del D., A. Mondini, B. Mazzolai, *Soft Robot.* **2020**, 7, 85.
- [10] J. D. Greer, L. H. Blumenschein, R. Alterovitz, E. W. Hawkes, A. M. Okamura, *Int. J. Robot. Res.* **2020**, 39, 1724.
- [11] A. Sadeghi, A. Mondini, B. Mazzolai, *Soft Robot.* **2017**, 4, 211.
- [12] J. D. Greer, T. K. Morimoto, A. M. Okamura, E. W. Hawkes, *Soft Robot.* **2019**, 6, 95.
- [13] P. Slade, A. Gruebele, Z. Hammond, M. Raitor, A. M. Okamura, E. W. Hawkes, in *Proc. of 2017 IEEE/RSJ Int. Conf. on Intelligent Robots and Systems (IROS)*, IEEE, Piscataway, NJ **2017**, pp. 174–180.
- [14] N. D. Naclerio, C. M. Hubicki, Y. O. Aydin, D. I. Goldman, E. W. Hawkes, in *Proc. 2018 IEEE/RSJ Int. Conf. on Intelligent Robots and Systems (IROS)*, IEEE, Piscataway, NJ **2018**, pp. 5918–5923.
- [15] B. Mosadegh, P. Polygerinos, C. Keplinger, S. Wennstedt, R. F. Shepherd, U. Gupta, J. Shim, K. Bertoldi, C. J. Walsh, G. M. Whitesides, *Adv. Funct. Mater.* **2014**, 24, 2163.
- [16] D. Yang, B. Mosadegh, A. Ainla, B. Lee, F. Khashai, K. Bertoldi Z. Suo, G. M. Whitesides, *Adv. Mater.* **2015**, 27, 6323.
- [17] L. Jin, A. E. Forte, K. Bertoldi, *Adv. Sci. Lett.* **2021**, 8, 2101941.

- [18] B. Gorissen, D. Melancon, N. Vasios, M. Torbati, K. Bertoldi, *Sci. Robot.* **2020**, 5, eabb1967.
- [19] E. Ben-Haim, L. Salem, Y. Or, A. D. Gat, *Soft Robot.* **2020**, 7, 259.
- [20] F. Connolly, C. J. Walsh, K. Bartholdi, *Proc. Natl. Acad. Sci. USA* **2017**, 114, 51.
- [21] N. P. Bende, T. Yu, N. A. Corbin, M. A. Dias, C. D. Santangelo, J. A. Hanna, R. C. Hayward, *Soft Matter* **2018**, 14, 8636.
- [22] P. Breitman, M. Pukshansky, A. Zigelman, S. Givli, A. D. Gat, *Phys. Rev. Lett.* **2022**, 18, 064077.
- [23] J. Hua, H. Lei, Z. Zhang, C. Gao, D. Fang, *J. Appl. Mech.* **2019**, 86, 071007.
- [24] K. Wei, Q. Yang, B. Ling, Z. Qu, Y. Pei, D. Fang, *Extreme Mech. Lett.* **2018**, 20, 51.
- [25] H. Yang, L. Ma, *J. Mater. Sci.* **2019**, 54, 3509.
- [26] J. Denavit, R. S. Hartenberg, *J. Appl. Mech.* **1955**, 22, 215.
- [27] O. Peretz, A. K. Mishra, R. F. Shepherd, A. D. Gat, *Proc. Natl. Acad. Sci. USA* **2020**, 117, 5217.
- [28] D. Melancon, A. E. Forte, L. M. Kamp, B. Gorissen, K. Bertoldi, *Adv. Funct. Mater.* **2022**, 32, 2201891.
- [29] P. Roy, L. Ashton, T. Wang, M. G. Corradini, E. D. G. Fraser, M. Thimmanagari, M. Tiessan, A. Bali, K. M. Saharan, A. K. Mohanty, M. Misra, *J. Clean. Prod.* **2021**, 316, 128234.